Supplement of Atmos. Chem. Phys., 26, 5635–5652, 2026
https://doi.org/10.5194/acp-26-5635-2026-supplement

Atmospheric Chemistry and Physics
Open Access
EGU

Supplement of

Measurement report: Ice nucleation ability of perthite feldspar powder

Julia Canet et al.

Correspondence to: Albert Verdaguer (averdaguer@icmab.es)

Mineral quarries and location fronts

Six feldspar minerals sourced from two industrial quarries were investigated for their ice-nucleating (IN) activity. The samples were provided by two industrial mineral companies: Imerys (France) and LLANSÀ, S.A. (Llançà, Catalonia, Spain).

Two K-rich feldspar samples were supplied by the French industrial minerals company Imerys and collected from different extraction fronts within active operations. These samples are designated ImerysK1 (IK1) and ImerysK2 (IK2). Although the company did not disclose the specific mine locations, both samples are known to originate from ongoing industrial extraction.

Four additional feldspar samples were obtained from the LLANSÀ, S.A. quarry. These feldspar powders are labeled LlançaNa1 (LNa1), LlançaNa2 (LNa2), LlançaNaK1 (LNaK1), and LlançaNaK2 (LNaK2). Depending on the extraction front, the samples include two predominantly Na-rich feldspars and two feldspars with approximately balanced Na/K compositions. Specifically, sample LNa2 originates from the SN extraction front, samples LNa1 and LNaK2 from the SE extraction front, and sample LNaK1 from the N extraction front. Photographs of the corresponding extraction fronts are shown in Fig. S1.

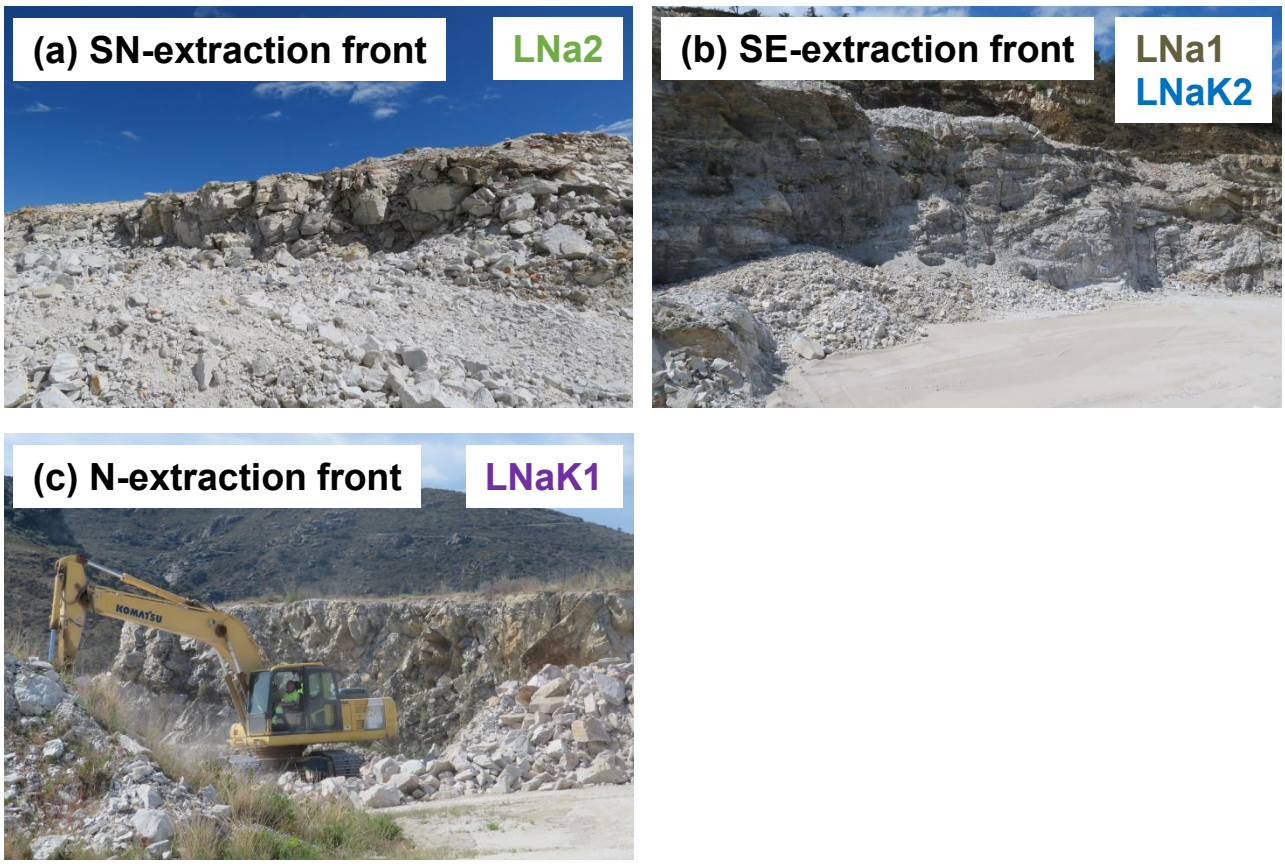

Figure S1. Pictures of the three extraction fronts of feldspars from LLANSÀ S.A. and the name of the sample obtained from each front. (a) SN-extraction front. (b) SE-extraction front. (c) N-extraction front.

Milling procedure

For the Llançà samples, representative portions of each bulk rock were crushed and homogenized using high-purity silica ball milling to produce fine powders. The production rate for all Llançà feldspar samples was 6 Tm h^{-1}, whereas the LNa2 'small particles' fraction was produced at 3 Tm h^{-1}, where Tm denotes metric tonnes. These powders were primarily prepared for ice nucleation experiments, and additionally used for granulometric, chemical, and mineralogical analyses.

Chemical and mineral composition

The chemical composition of the feldspar samples was determined using a Philips PW 2400 X-ray fluorescence (XRF) sequential spectrometer located at the Centres Científics i Tecnològics de la Universitat de Barcelona (CCiT-UB). Major oxides (expressed as weight percent) were quantified via the fused bead method, while trace elements (in ppm) were measured using pressed powder pellets (see Table S1 and S2). Quantification was calibrated against certified geological standards to ensure analytical accuracy. In addition, thermal treatments were conducted to assess Loss on Ignition [ASTM D7348-21].

Mineralogical characterization was conducted through a combination of X-ray diffraction (XRD), Optical Microscope (OM), and Scanning Electron Microscope (SEM). XRD measurements were performed on a PANalytical X'Pert System diffractometer, configured in Bragg-Brentano geometry with Cu Kα radiation ($\lambda = 1.54061$ Å). Phase identification and semi-quantitative analysis were conducted with the XPert Graphics Identify software (Philips). For microstructural and petrographic examination, double-polished thin sections were observed using a Nikon ACT-1 optical microscope. The same sections were examined using a Hitachi TM-1000 tabletop SEM, coupled with energy-dispersive X-ray spectroscopy (EDS) to analyze microstructural features and verify elemental composition.

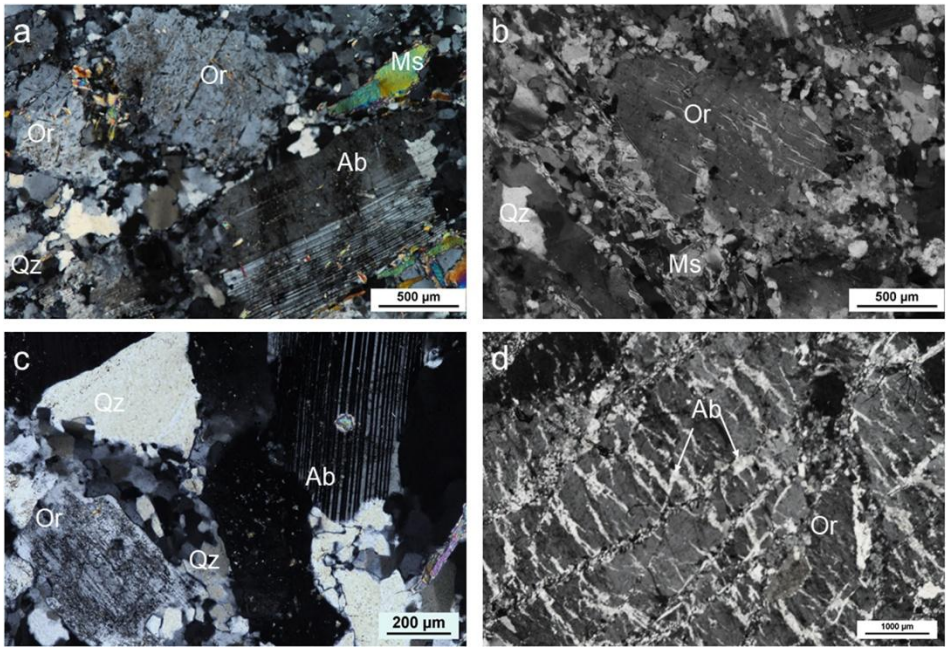

Figure S2. Photomicrographs (under crossed polars) corresponding to three exploration levels of the pegmatitic feldspars from Llançà. (a) Granular texture formed by a large euhedral albite crystal showing polysynthetic twinning and an hemihedral orthoclase crystal, surrounded by small anhedral quartz and muscovite crystals. (b) The central part shows an hemihedral orthoclase crystal with microperthite texture surrounded by quartz. (c) Euhedral albite (polysinthetic twining) and orthoclase being altered to kaolinite and sericite accompanied with several sizes of quartz grains. (d) Perthitic texture shows fine lamellar albite crystals forming a braided pattern in an orthoclase host. Abbreviations: Ab, albite; Ms, muscovite; Or, orthoclase; Qz, quartz.

Table S1. Bulk chemical composition of the studied feldspars, expressed as wt% oxides determined by X-ray fluorescence (XRF). Oxide ratios (K_2O/Na_2O and SiO_2/Al_2O_3) and Loss on ignition (LOI) are also reported.

Sample name	Texture	Main polymorph	SiO_2	Al_2O_3	Na_2O	K_2O	CaO	K_2O/Na_2O	SiO_2/Al_2O_3	MgO	Fe_2O_3	TiO_2	P_2O_5	LOI
IK1	Perthitic	Mc	64.97	18.81	2.95	12.78	0.32	4.3	3.4	0.03	0.06	0	0.07	–
IK2	Perthitic	Mc	65.84	18.76	3.31	11.86	0.1	3.6	3.5	0.01	0.1	0	0.01	0.19
LNaK1	Perthitic	Or/Mc	75.18	14.85	3.67	3.78	0.79	1.0	5.1	0.17	0.62	0.08	0.29	0.83
LNaK2	Perthitic	Or/Mc	73.23	15.30	5.13	4.83	0.65	0.9	4.8	0.06	0.11	0.01	0.31	0.38
LNa1	Anti-perhtitic	Ab	75.67	14.17	5.91	2.27	0.73	0.4	5.3	0.07	0.14	0.02	0.30	0.35
LNa2	Anti-perhtitic	Ab	75.71	14.46	6.84	1.38	0.75	0.2	5.2	0.07	0.15	0.02	0.30	0.44

Table S2. Trace elements concentration (in ppm) measured using X-ray fluorescence (XRF) for the feldspar powders. Values reported as <ld indicate concentrations below the detection limit. Rb and Sr values are highlighted in red due to their direct mention in the main text.

ppm	IK1	IK2	LNaK1	LNaK2	LNa1	LNa2
As	3.7	< ld	< ld	1.96	< ld	< ld
Ba	60.1	59.5	141.7	314.1	147.8	116.3
Ce	< ld	< ld	6.7	< ld	< ld	< ld
Co	< ld	< ld	< ld	69.6	< ld	< ld
Cr	< ld	< ld	< ld	< ld	< ld	< ld
Cu	5	1.5	1.2	< ld	0.3	0.2
Ga	11.1	28.9	24.5	16.2	20.7	20.0
La	< ld	1.8	< ld	< ld	< ld	< ld
Mo	0.2	< ld	< ld	< ld	< ld	< ld
Nb	8.9	9.1	16.7	19.3	13.9	13.1
Nd	< ld	< ld	< ld	< ld	< ld	< ld
Ni	1.7	< ld	< ld	< ld	< ld	< ld
Pb	187.5	9.2	34.3	8.2	14.0	14.6
Rb	839.2	607.2	181.9	159.3	102.4	64.5
Sc	< ld	< ld	2.4	< ld	< ld	< ld
Sn	5.2	< ld	13.1	5.0	5.7	4.6
Sr	25.2	26.6	54.9	132.9	92.6	78.8
Th	2.6	3.3	4.1	2.7	3.2	2.9
V	4.8	4.3	8.8	5.7	6.6	6.1
W	< ld	11.4	1.4	575.1	< ld	< ld
Y	24	17.8	14.2	7.4	8.2	7.2
Zn	61.5	51.3	8.1	53.8	36.3	41.0
Zr	37.1	33.1	261.9	36.4	42.2	42.1
Ag	< ld	< ld	< ld	< ld	< ld	< ld
Bi	5.1	5.2	6.0	4.6	5.1	5.2
Br	2.2	1.8	2.4	6.1	2.3	2.0
Cd	< ld	< ld	0.7	< ld	< ld	< ld
Cs	42.3	0.1	10.0	< ld	5.6	3.3
Ge	7	6.7	1.8	5.4	2.3	2.7
Hf	10.7	9.6	5.6	10.9	8.5	6.6
Hg	61.5	63.3	25.4	< ld	25.0	35.3
I	< ld	< ld	1.7	< ld	2.6	2.5
Mn	41.2	32.7	250.3	41.0	115.1	116.8
Sb	1.9	1.3	1.0	2.4	2.2	2.2
Se	0.2	0.1	0.1	< ld	0.3	< ld
Sm	< ld	2.5	0.4	< ld	1.4	0.9

Ta	2.5	1.9	3.8	9.5	3.5	3.2
Te	0.2	< ld	-0.3	0.5	2.0	< ld
Tl	3.7	2.1	2.5	1.2	1.1	1.2
U	4.3	4.2	6.8	2.7	7.7	6.0
Yb	7	3.2	5.0	5.6	5.6	4.2

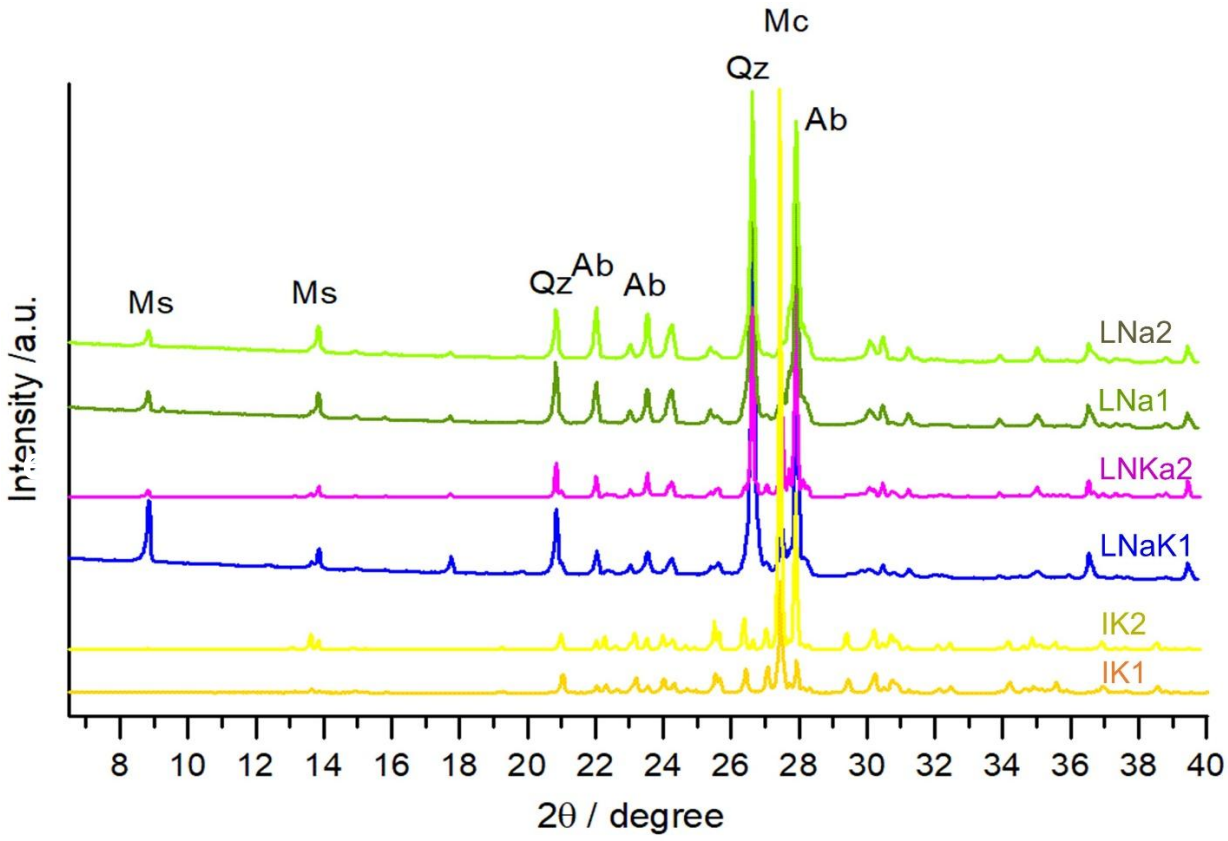

Figure S3. X-ray diffraction (XRD) spectra for all feldspar powders: IK1, IK2 (K-rich); LNaK1, LNaK2 (K/Na); and LNa1, LNa2 (Na-rich). The analysis was performed over the 2θ range of 8-40°. Identified phases include: mica (Ms), quartz (Qz), albite (Ab), and microcline (Mc).

Immersion freezing assays

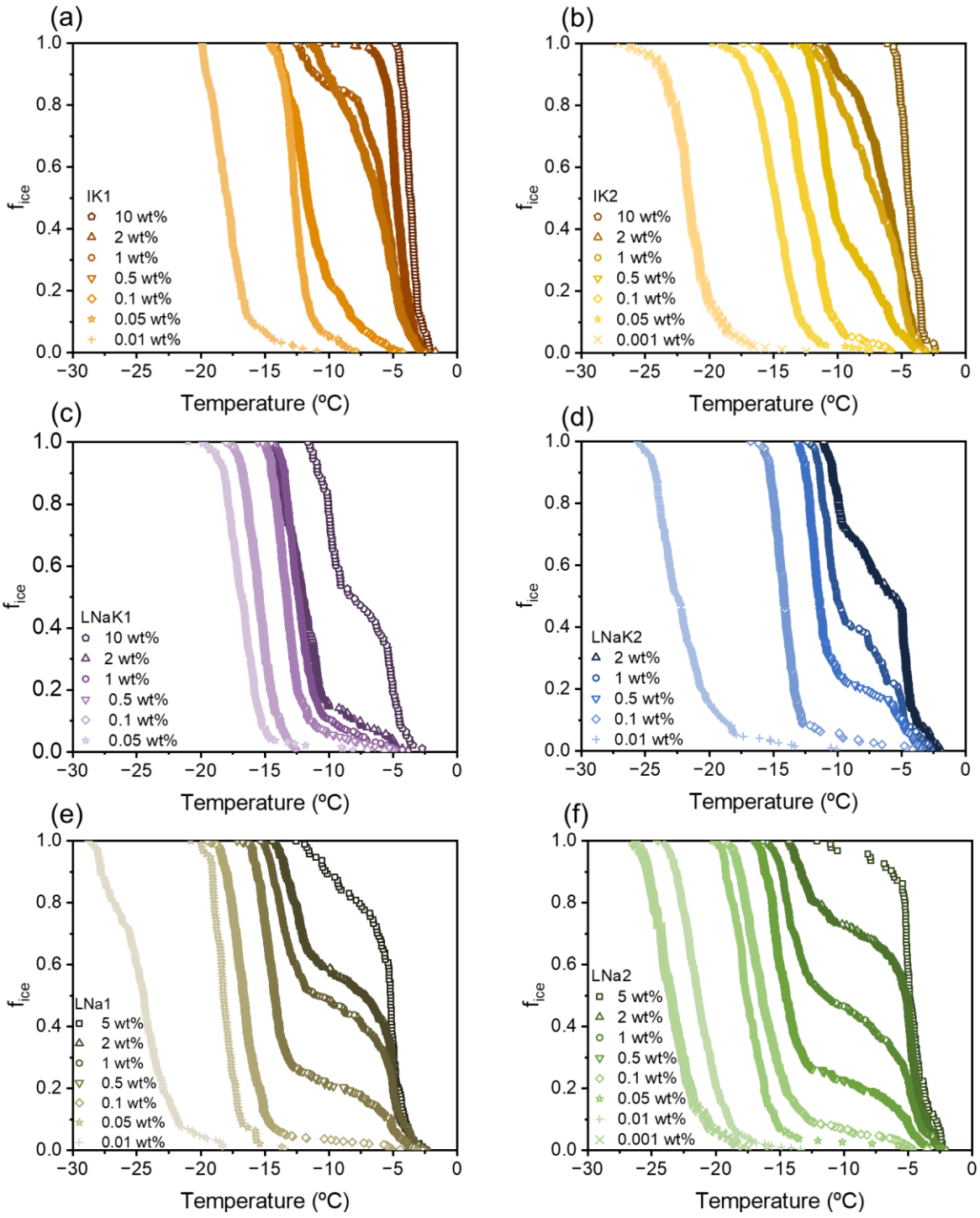

Figure S4. Fraction of frozen droplets, $f_{\mathrm{ice}}(T)$, for all feldspar samples and concentrations tested. Panels correspond to: (a) IK1, (b) IK2, (c) LNaK1, (d) LNaK2, (e) LNa1, and (f) LNa2.

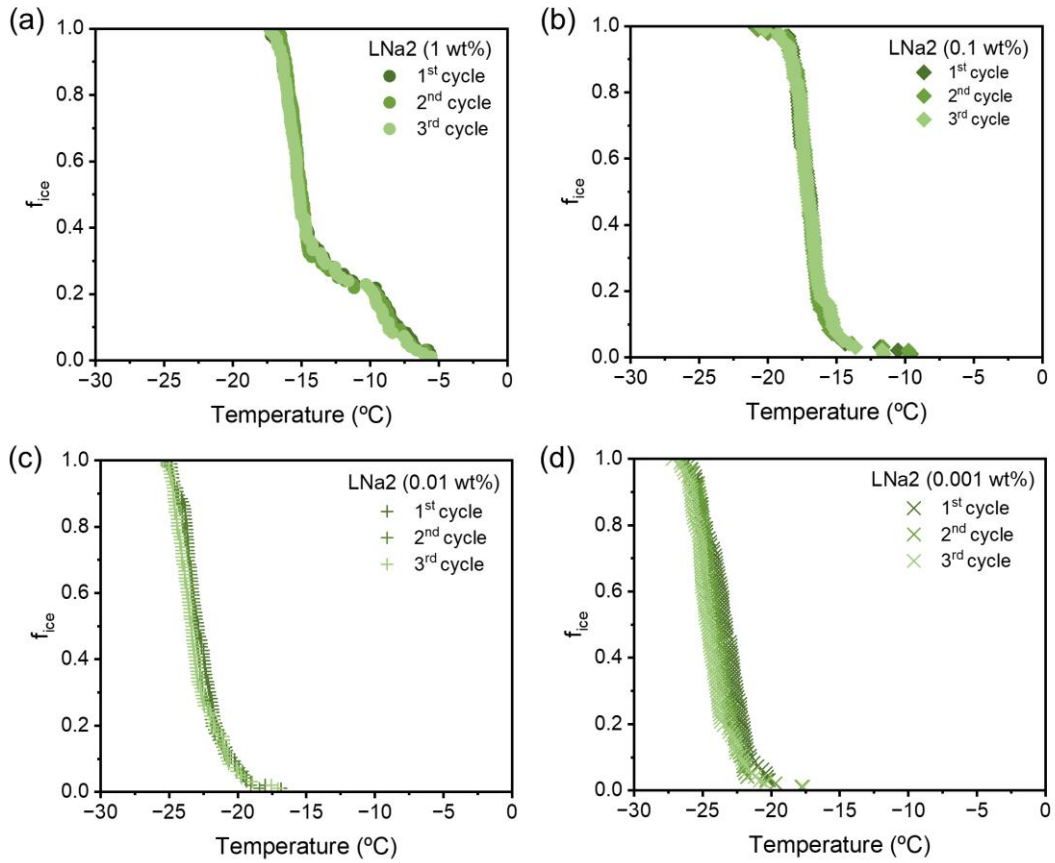

Figure S5. Freezing spectra of LNa2 feldspar suspensions at different concentrations. The fraction of frozen droplets, $f_{\mathrm{ice}}(T)$, measured over three successive freeze-thaw cycles shows no significant variation, indicating stable IN behavior. Panels show: (a) 1 wt%, (b) 0.1 wt%, (c) 0.01 wt%, and (d) 0.001 wt%.

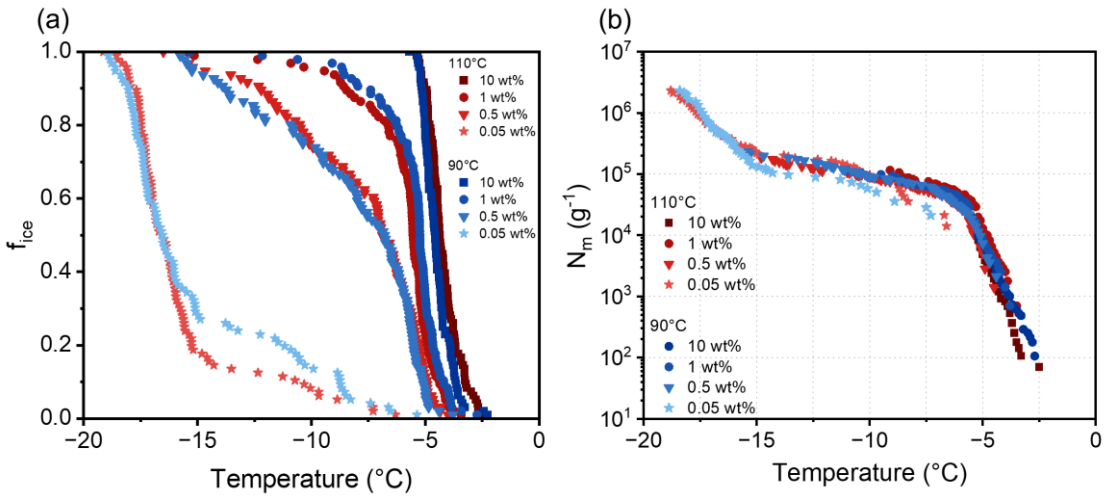

Figure S6. Immersion freezing assays of aqueous LNa suspensions (10, 1, 0.5, and 0.05 wt%) after heat treatment. The fraction of frozen droplets, $f_{\mathrm{ice}}(T)$, was measured after heating the suspensions at 90 °C and 110 °C for 30 min to assess the potential contribution of biological IN contaminants. No changes in $f_{\mathrm{ice}}(T)$ were observed after heating, indicating that biological contamination is unlike under these temperature and time conditions. (a) Fraction of frozen droplets, $f_{\mathrm{ice}}(T)$. (b) Cumulative ice-nucleating site density per unit mass, $N_{\mathrm{m}}(T)$.

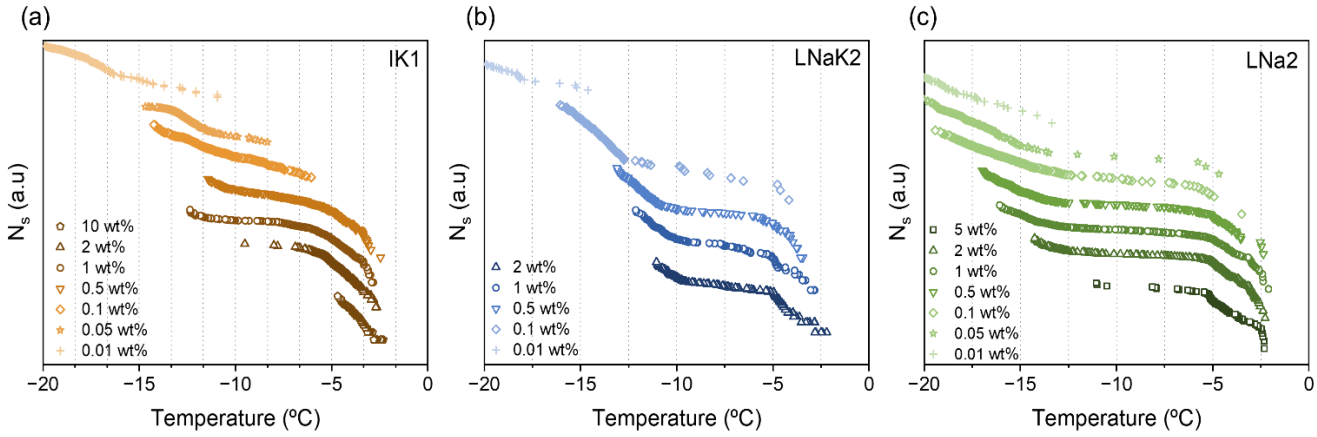

Figure S7. Ice-nucleating active site density, $N_s(T)$, as a function of temperature for different feldspar suspensions. Curves are vertically offset to aid visualization and comparison of the freezing spectra. (a) IK1. (b) LNaK2. (c) LNa2.

HUB analysis

Table S3. Averaging values for the first 10 freezing events, $T_{(i,10)}$, for each feldspar suspension: IK1, IK2, LNaK1, LNaK2, LNa1, LNa2.

	IK1		IK2		LNaK1		LNaK2		LNa1		LNa2	
	wt%	T (ºC)	wt%	T (ºC)	wt%	T (ºC)	wt%	T (ºC)	wt%	T (ºC)	wt%	T (ºC)
	10	-2.17	10	-2.39	10	-3.44	2	-1.95	1	-2.35	1	-2.10
	10	-2.18	10	-2.41	10	-3.67	2	-2.20	1	-2.50	2	-2.28
	10	-2.25	10	-2.50	10	-3.74	2	-2.210	1	-2.65	5	-2.31
	10	-2.31	10	-3.06	2	-3.83	2	-2.21	0.5	-2.68	5	-2.32
	10	-2.39	1	-3.09	10	-3.97	2	-2.44	5	-2.71	0.5	-2.37
	2	-2.41	2	-3.15	10	-3.98	2	-2.50	2	-2.79	1	-2.38
	10	-2.44	2	-3.17	1	-4.22	1	-2.68	1	-2.79	2	-2.39
	0.5	-2.46	1	-3.18	10	-4.25	2	-2.77	2	-2.82	5	-2.39
	1	-2.57	1	-3.21	1	-4.27	2	-2.78	2	-2.93	1	-2.41
	10	-2.62	10	-3.26	2	-4.28	2	-2.79	5	-2.97	5	-2.41
$T_{(i,10)}$ (ºC)		-2.38		-2.94		-3.96		-2.45		-2.72		-2.33

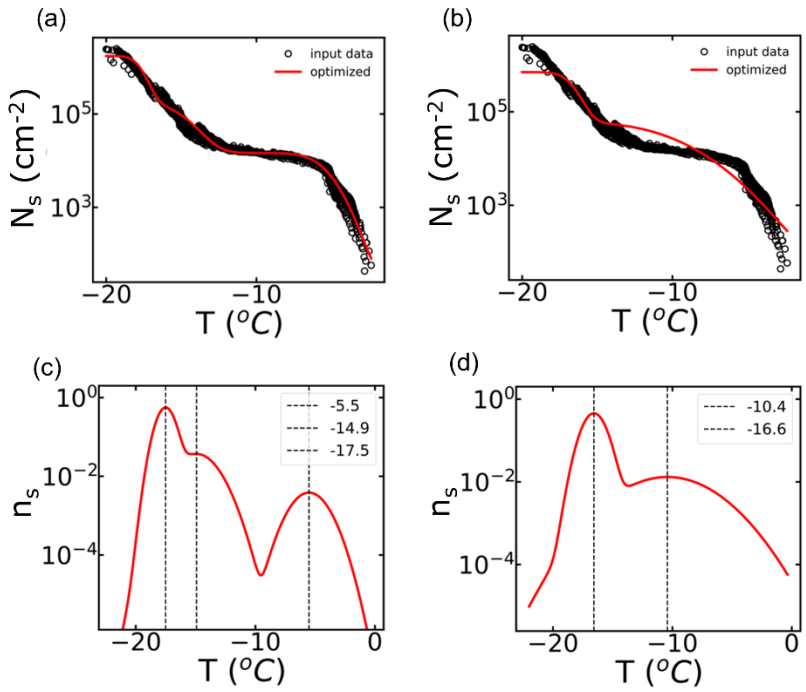

Figure S8. Subpopulation analysis of freezing experiments of the LNa1 feldspar suspension using HUB method (de Almeida et al., 2023). Top panels: cumulative active-site density, $N_s(T)$, (black circles) with HUB-backwards fits (red continuous lines) using (a) three, and (b) two subpopulations. Bottom panels: corresponding normalized differential spectra, $n_s(T)$, where (c) corresponds to three-subpopulation model and (d) to the two-subpopulation model. Vertical dashed lines indicate the mode temperatures (T_{mode}) of each subpopulation. The three-subpopulation model reproduces the freezing onset and overall spectral shape more accurately, yielding a lower mean squared error (MSE = 0.0041) than the two-subpopulation model (MSE = 0.0652). Accordingly, the three-subpopulation fit was selected for subsequent analyses. Fit parameters are reported in Table S4.

Table S4. Parameters of the normalized distribution functions obtained from the HUB subpopulation analysis of the LNa1 feldspar freezing spectra shown in Fig. S8, using three and two subpopulations. Listed are the temperatures of the corresponding subpopulation, and the probability of a droplet to freeze from each subpopulation. The mean squared error (MSE) describes the quality of the found optimized solution for the cumulative spectra obtained with the HUB analysis relative to the experimental cumulative spectra.

	Subpopulations	SubP-A		SubP-B		SubP-C		MSE
		T (°C)	%	T (°C)	%	T (°C)	%	
LNa1	3	-5.51	1.16	-14.9	12.58	-17.51	86.26	0.0041
	2	-10.4	10.0	-16.57	90.0	-	-	0.0652

Table S5. Temperatures corresponding to the subpopulations of the differential freezing spectra shown in Fig. 4 and the probability of a droplet to freeze from each subpopulation. Note: Probability has been calculated assuming that all droplets are frozen at -20 °C which is the case for densities below or approximately 0.01.

	SubP-A		SubP-B		SubP-C		MSE
	T (°C)	%*	T (°C)	%	T (°C)	%	
IK1	-5.4	0.3	-13.1	10.9	-17.4	88.7	0.0068
IK2	-6.1	0.8	-13.5	18.0	-16.4	81.2	0.0075
LNaK1	-5.7	0.2	-14.1	10.4	-16.5	89.4	0.0045
LNaK2	-5.6	0.4	-14.0	24.9	-16.0	74.61	0.0095
LNa1	-5.5	1.2	-15	12.6	-17.5	86.3	0.0041
LNa2	-5.5	0.8	-15.4	16.7	-18.0	82.4	0.0138

Table S6. Parameter of the normalized distribution functions of the freezing obtained through HUB method using three Gaussian subpopulations of perthites published by Whale et al. (2017): Orthoclase perthites (Dark Shap, Light Shap and LD4); Microcline perthites (KB14, Perthite, Keystone); and from Harrison et al. (2016): nearly pure albite and microcline. Temperatures of the corresponding subpopulation, and the probability of a droplet to freeze from each subpopulation. The mean squared error (MSE) describes the quality of the found optimized solution for the cumulative spectra obtained with the HUB analysis relative to the experimental cumulative spectra.

	SubP-A		SubP-B		SubP-C		MSE
	T (°C)	%*	T (°C)	%	T (°C)	%	
Dark Shap	-4	8.5	-11.9	20.2	-14.9	71.3	0.0035
Light Shap	-6.0	4.7	-13.9	19.4	-17.5	75.9	0.0063
LD4	-6.0	5.5	-14.5	25.8	-17.2	68.7	0.0085
KB14	-7.1	11.3	-12	41.3	-14.0	47.4	0.0033
Perthite	-6.1	5.5	-10.0	27.1	-13.0	67.5	0.0014
Keystone	-7.7	0.1	-11.3	14.1	-14.1	86.0	0.0029

Table S7. Parameters of the normalized distribution functions of the freezing obtained through HUB method (de Almeida, 2023) using two or three Gaussians subpopulations of feldspar suspensions published by Kiselev et al. (2021): FS08-VS 1 wt% (untreated Volkesfeld sanidine), FS08-64c (albite-shifted sanidine tempered at 550 ºC for 64 days in vacuum), FS08-64o (albite-shifted sanidine tempered at 550 ºC for 64days in NaCl-KCl salt mixture melt). Temperatures of the corresponding subpopulation, and the probability of a droplet to freeze from each subpopulation. The mean squared error (MSE) describes the quality of the found optimized solution for the cumulative spectra obtained with the HUB analysis relative to the experimental cumulative spectra.

	SubP-A		SubP-B		SubP-C		MSE
	T (ºC)	%*	T (ºC)	%	T (ºC)	%	
FS08-64c	-14.4	11.4	-18.0	88.6	-	-	0.002
FS08-64o	-6.7	2.3	-15.3	10.9	-20.5	86.8	0.0034
FS08-VS	-19.7	26.8	-23.6	73.2	-	-	0.0046

References

de Almeida Ribeiro, I., Meister, K., and Molinero, V.: HUB: a method to model and extract the distribution of ice nucleation temperatures from drop-freezing experiments, Atmos. Chem. Phys., 23, 5623-5639, https://doi.org/10.5194/acp-23-5623-2023, 2023.

Harrison, A. D., Whale, T. F., Carpenter, M. A., Holden, M. A., Neve, L., O'Sullivan, D., Vergara Temprado, J., and Murray, B. J.: Not all feldspars are equal: A survey of ice nucleating properties across the feldspar group of minerals, Atm. Chem. Phys., 16, 10927-10940, https://doi.org/10.5194/acp-16-10927-2016, 2016.

Kiselev, A. A., Keinert, A., Gaedeke, T., Leisner, T., Sutter, C., Petrishcheva, E., and Abart, R.: Effect of chemically induced fracturing on the ice nucleation activity of alkali feldspar, Atmos. Chem. Phys., 21, 11801-11814, https://doi.org/10.5194/acp-21-11801-2021, 2021.

Whale, T. F., Holden, M. A., Kulak, A. N., Kim, Y. Y., Meldrum, F. C., Christenson, H. K., and Murray, B. J.: The role of phase separation and related topography in the exceptional ice-nucleating ability of alkali feldspars, PCCP, 19, 31186-31193, https://doi.org/10.1039/c7cp04898j, 2017.